

1 **Revision 1**

2 **Gamma-enhancement of reflected light images as a routine method for assessment**  
3 **of compositional heterogeneity in common low-reflectance Fe-bearing minerals**

4 QIAOQIAO ZHU<sup>1</sup>, GUIQING XIE<sup>2,\*</sup>, NIGEL J. COOK<sup>3</sup>, CRISTIANA L. CIOBANU<sup>3</sup>, HUI WANG<sup>4</sup>

5 <sup>1</sup> *MNR Key Laboratory of Metallogeny and Mineral Assessment, Institute of Mineral Resources, CAGS,*

6 *Beijing 100037, China*

7 <sup>2</sup> *MNR Key Laboratory for Exploration Theory & Technology of Critical Mineral Resources, School of*

8 *Earth Sciences and Resources, China University of Geosciences, Beijing 100083, China*

9 <sup>3</sup> *School of Chemical Engineering, The University of Adelaide, Adelaide, SA 5005, Australia*

10 <sup>4</sup> *School of Earth Science and Resources, Chang'an University, Xi'an 710054, China*

---

11 **ABSTRACT**

12 Incorporation of impurity elements into minerals impacts on their physical properties (e.g., reflectance,  
13 hardness, and electrical conductivity) but the quantitative relationships between these features and  
14 compositional variation remain inadequately constrained. Prior work has shown that  
15 gamma-enhancement of reflected light images represents a simple yet powerful tool to assess the  
16 compositional heterogeneity of single pyrite crystals as it can enhance subtle differences in reflectance  
17 between distinct domains with different minor element concentrations. This study extends the gamma  
18 correction method to several other common Fe-bearing minerals, magnetite, garnet, wolframite, and

---

\*Corresponding author: Dr. Guiqing Xie, E-mail: [xieguiqing@cugb.edu.cn](mailto:xieguiqing@cugb.edu.cn)

19 tetrahedrite-tennantite, which all have far lower reflectance than pyrite. Gamma-enhanced optical  
20 images reveal clear variations in reflectance that are either systematic with increased minor element  
21 concentration as the change in gray value on backscatter electron (BSE) images (in the case of magnetite,  
22 garnet, and tetrahedrite-tennantite) or contrasting (as in pyrite), yielding a convincing linkage between  
23 reflectance variation and compositional heterogeneity. Reflectance variation is an expression of the  
24 distribution of the average effective number of free electrons on the mineral surface that can re-emit  
25 light when excited by visible light. Gamma-enhanced images can reveal compositional heterogeneity in  
26 minerals such as wolframite where small atomic mass differences between substituting elements (Mn  
27 and Fe, in the case of wolframite) are virtually impossible to observe as a variation of gray values on  
28 BSE images. Results also demonstrate that Fe-rich domains in these minerals can be expected to have  
29 higher reflectance than Fe-poor domains whenever Fe is a major constituent. The greater reflectance is  
30 attributed to Fe ions having a greater effective number of free electrons than many other elements (e.g.,  
31 Co, Ni, Si, Ca, Al, Mg, Mn, and As). The research highlights the utility of gamma correction as an  
32 inexpensive tool for routine evaluation of compositional heterogeneity in common Fe-bearing minerals,  
33 potentially obviating the necessity of a microbeam platform to correlate textures and composition.

34 **Keywords:** Gamma correction; compositional homogeneity; reflectance; magnetite; garnet; wolframite;  
35 tetrahedrite-tennantite.

---

## INTRODUCTION

36

37 Many minerals display variable compositions and deviate from ideal stoichiometry due to the presence  
38 of different levels of impurities induced by solid solution exchange reactions or the presence of discrete  
39 nanoscale mineral inclusions (e.g., [Craig and Vaughan 1994](#); [Cook et al. 2016](#); [Ciobanu et al. 2019](#)).  
40 Such variation can modify the physical features of minerals, such as reflectance, hardness, Raman  
41 spectra, and electrical conductivity and may also significantly impact the behavior of a mineral during  
42 ore processing (e.g., [Craig and Vaughan 1994](#); [Abraitis et al. 2004](#); [Buzatu et al. 2013](#); [Galili et al. 2023](#)).  
43 For example, arsenic-rich pyrite exhibits low conductivity, reflectance, and Raman band positions  
44 whereas As-poor varieties have relatively higher corresponding features ([Saager and Mihálik 1967](#);  
45 [Abraitis et al. 2004](#); [Zhu et al. 2020, 2021](#)). In addition, systematic variation of physical features  
46 (reflectance, multispectral reflectance, and Raman spectra) have been observed as a function of  
47 composition ([Craig and Vaughan 1994](#); [López-Benito et al. 2017](#); [Zhu et al. 2020, 2023](#); [Berkh and](#)  
48 [Rammlmair 2022](#); [Galili et al. 2023](#)). Furthermore, distinct elements in the same mineral may yield  
49 varied physical features. In sphalerite, for example, Fe was suggested to affect Raman band positions at  
50  $\sim 350\text{ cm}^{-1}$  and  $300\text{ cm}^{-1}$  while Cd was assigned to related to a new band position at  $\sim 295\text{ cm}^{-1}$  ([Babedi et](#)  
51 [al. 2019](#)). Thus, some specific physical features of minerals have the potential to be used as effective  
52 tools to estimate variation in chemical composition without the need for costly and time-consuming  
53 electron microprobe analysis. This type of method may thus represent a rapid, user-friendly approach to  
54 semi-quantitatively assess the chemical composition of mineral on-site or in outcrop long before any  
55 laboratory-based testing is carried out ([Jehlička and Culka 2022](#)). Estimates of variation in chemical

3

56 composition can, in turn, provide critical information on the spatial-temporal evolution of a mineral  
57 assemblage or the conditions of its formation or superimposed events. In processing plants,  
58 compositional data, especially information on valuable or penalty impurity elements, will assist in  
59 prediction and optimization of downstream behavior and metallurgical performance.

60 Several detailed investigations have suggested that reflectance values of some ore minerals (e.g.,  
61 pyrite, ilmenite, and galena) are sensitive to compositional variation and have developed rapid  
62 method(s) to determine the specific compositions based on their reflectance variation ([Saager and](#)  
63 [Mihalik 1967](#); [Vaughan 1969](#); [Tarkian 1987](#); [Craig and Vaughan 1994](#)). These methods have, however,  
64 been in decline since the 1990s due to the lamentable decline in the training and use of reflected light  
65 microscopy on a routine basis, as well as two other reasons. Firstly, reflectance variation caused by  
66 compositional heterogeneity within minerals is commonly subtle, especially for minerals with  
67 relatively low reflectance, and thus can be invisible in conventional polished sections viewed in  
68 reflected light, at least without oil immersion ([Craig and Vaughan 1994](#); [Craig 2001](#)). Secondly,  
69 reflectance data are less definitive than a chemical composition determined by microbeam methods  
70 ([Stanley 2013](#)). [Pačevski \(2007\)](#) noted that computer-adjusted reflected light images with increased  
71 contrast and decreased brightness are useful to observe grain-scale compositional zoning in wolframite.  
72 This preliminary research shows an encouraging advantage over back-scattered electron (BSE)  
73 imaging in textural characterization of wolframite. [Zhu et al. \(2021, 2022\)](#) noted gamma correction of a  
74 reflected light image can enhance reflectance variation between different domains in pyrite and is a  
75 robust tool to address the compositional heterogeneity of pyrite at grain scale. This method also

76 belongs to the digital image processing technology and represents an important advance (e.g.,  
77 non-destructive and reproducible) over traditional techniques (e.g., chemical etching and straining)  
78 which were widely used to characterize compositional heterogeneity and ore textures prior to the  
79 advent of scanning electron microscope and microprobe analysis as routine characterization techniques  
80 (e.g., [Ramdohr 1969](#); [Fleet et al. 1993](#); [Gregory et al. 2016, 2019](#)). Gamma correction may be easily  
81 conducted on most optical microscopes, requires no special training, and is non-destructive. Recently,  
82 we found this method could also be used to routinely characterize ore minerals with relatively lower  
83 reflectance and even (semi-)transparent gangue minerals, which are expected to show still subtler  
84 reflectance variation induced by the change of composition. Lastly, we note that the general  
85 relationship between an increase or decrease in reflectance and compositional variation tied to specific  
86 elements has yet to be addressed for many minerals and mineral groups.

87 There are more than 1000 iron-bearing minerals included in common mineralogy databases (e.g., the  
88 [webmineral.com](http://webmineral.com) Mineralogy Database or the [mindat.org](http://mindat.org) database), formed at a wide range of  
89 temperatures and pressures and stable in deep mantle, shallow crustal, and surface environments. The  
90 reflectance of some major Fe-bearing minerals (e.g., ilmenite, pyrite, and chromite) has been shown to  
91 be sensitive to variation in composition ([Vaughan 1969](#); [Cervelle et al. 1971](#); [Eales 1980](#); [López-Benito](#)  
92 [et al. 2017](#); [Zhu et al. 2021](#)). Published reflectance values for these Fe-bearing minerals span a broad  
93 range from <10% to >50% and often exhibit variability in reflectance which may be induced by impurity  
94 incorporation ([Criddle and Stanley 1993](#); [Craig and Vaughan 1994](#)). Therefore, Fe-bearing minerals are  
95 ideal candidates to explore relationships between change in reflectance and compositional variation,

96 especially in single mineral grains displaying compositional homogeneity. In this contribution, we use  
97 the gamma correction method to investigate the relationship between optical features and compositional  
98 variation in four common Fe-bearing minerals: magnetite (~69 wt% Fe); garnet (~19 wt% Fe);  
99 wolframite (~7 wt% Fe), and tetrahedrite-tennantite (~1.70 wt% Fe). The results suggest that both solid  
100 solution exchange and sub- micron-sized mineral inclusions contribute to the grain-scale compositional  
101 heterogeneity causing reflectance variation highlighted in gamma-enhanced reflected images. This study  
102 further highlights the potential of gamma-corrected reflected light images as a routine method to assess  
103 compositional heterogeneity in common, low reflectance Fe-bearing minerals.

#### 104 **SAMPLING AND METHODOLOGY**

105 The magnetite-bearing sample (JS42) was collected from the Jinshandian Fe skarn deposit, Edong  
106 district, eastern China, which occurs at the contact between the 130–127 Ma Jinshandian pluton and  
107 Triassic units (Zhu et al. 2015, 2017). Magnetite is the main ore mineral and is associated with  
108 phlogopite. Pyrite and anhydrite commonly occur interstitial to magnetite grains or crosscut them. Prior  
109 scanning electron microscope (SEM) imaging suggests that some magnetite grains from Jinshandian  
110 display two stages of overgrowth although these are hardly visible under reflected light (Fig. 1, Zhu et al.  
111 2019).

112 The garnet-bearing sample (FJ279-1) was collected from the Fujiashan W-Cu-Mo skarn deposit,  
113 Edong district, eastern China, located at the contact between the Late Mesozoic granodiorite porphyry  
114 stock (~144 Ma; Ding et al. 2014) and Carboniferous to Triassic carbonate rocks (Ji et al. 2019).  
115 Metasomatism is characterized by a thick exoskarn predominantly composed of garnet and minor

116 diopside, vesuvianite, epidote, amphibolite, and wollastonite (Zhu et al. 2023). Compositional  
117 heterogeneity of garnet is well preserved and is indicated by a color change from red-brown to light  
118 brown or greenish red brown in hand specimens and gray values of BSE images (Fig. 2).

119 The wolframite-bearing sample (19XLK57) was collected from the Xingluokeng porphyry W deposit,  
120 Wuyishan metallogenic belt, eastern China. Ores occur at the roof of a biotite granite porphyry (~152.5  
121 Ma, Wang et al. 2021a). Wolframite and scheelite are the main ore minerals (~1:1) and are distributed as  
122 veinlet-disseminated, stockwork, and vein-type mineralization. Two stages of wolframite are recognized,  
123 associated with early K-feldspar +scheelite +beryl, and later sulfides (chalcopyrite, sphalerite, and pyrite)  
124 +scheelite +Fe-dolomite, respectively (Fig. 3, Wang et al. 2021b).

125 The sample containing tetrahedrite-tennantite (JJW94) was collected from the Chengmenshan  
126 porphyry-skarn Cu deposit, Jiurui district, eastern China. Orebodies occur within the ~146 Ma  
127 granodiorite porphyry stock and along the contact zone between the intrusion and marine  
128 limestone/dolomite of Permian or Tertiary age (Xu et al. 2021). Copper ores from Chengmenshan are  
129 sub-divided into three types according to their location. Sample JJW94 is representative of  
130 carbonate-replacement ore occurring within the sedimentary carbonate rocks (Guo et al. 2021). The  
131 sample is composed of assimilated sulfides and tetrahedrite-tennantite in a matrix of carbonate minerals.  
132 Tetrahedrite-tennantite is associated with chalcopyrite and bornite, and to a less extent, with sphalerite,  
133 galena, and pyrite (Fig. 4).

134 All samples were prepared as 1-inch-diameter polished blocks or polished thin sections. Optical  
135 observation, SEM imaging, and electron microprobe analysis (EMPA) were performed at MNR Key

136 Laboratory of Metallogeny and Mineral Assessment, Institute of Mineral Resources, CAGS. Detailed  
137 textural observation on minerals was performed under reflected light in air using an Olympus BX51  
138 Petrographic Microscope. Grains with subtle reflectance variation were chosen to obtain optical digital  
139 images at higher magnification (20X, 50X) and conducted gamma correction. Background information  
140 on gamma correction can be found in [Zhu et al. \(2021\)](#) and is also described in Online Material  
141 Appendix A<sup>1</sup>. The operating procedures using different types of software linked to commonly used  
142 optical microscopes can refer to our previous research ([Zhu et al. 2021](#)). In this study,  
143 gamma-enhancement of reflected light images was refined using the gamma correction function of the  
144 NIS-Elements viewer (version 5.21.00) software. The  $\gamma$  parameter is constant at 10 in this study, the  
145 same as used by [Zhu et al. \(2021\)](#). The green channel was chosen as the principal color to display the  
146 gamma-enhanced images. Green channel intensity of linear profiles on reflected images of magnetite  
147 and garnet were measured before and after gamma correction by using the intensity profile function of  
148 ZEISS ZEN (version 2.1) software. Following gamma enhancement, the samples were coated with  
149 carbon and examined via spot analysis using a JXA-iHP200F Hyper Probe equipped with an  
150 energy-dispersive spectrometer (EDS) to evaluate grain-scale compositional heterogeneity. Quantitative  
151 mineral compositional data were also obtained using a JXA-iHP200F Hyper Probe microanalyzer.  
152 Analytical conditions are described in Online Material Appendix A<sup>1</sup>

153

## RESULTS

---

<sup>1</sup> Deposit item



## 154 **Variation of reflectance and geochemistry**

155 Mineral textures observable in reflected light images before and after gamma enhancement are  
156 illustrated in [Figs. 1–4](#); corresponding EMPA data are listed in [Tables 1–4](#) and plotted in [Fig. 5](#).  
157 Magnetite grains (Jinshandian sample) display core and rim textures under reflected light. Core domains  
158 (Mag1) are slightly brighter than their rims (Mag2) in reflected light, especially when viewed under high  
159 magnification ([Fig. 1a](#)). This feature is manifested in gamma-enhanced images which reveal the  
160 irregular nature of the domain boundary ([Fig. 1b](#)). Optical heterogeneity of some rims is also exposed in  
161 the gamma-enhanced images whereby some domains (Mag2D) appear slightly darker than others  
162 (Mag2L, [Fig. 1b](#)). The differences in reflectance between distinct magnetite domains in the  
163 gamma-enhanced images are mirrored by the change in gray values on BSE images ([Fig. 1c](#)). EMPA  
164 data ([Table 1](#)) show that the magnetite rim has greater SiO<sub>2</sub> (1.97–3.45 wt%), CaO (0.73–1.14 wt%),  
165 Al<sub>2</sub>O<sub>3</sub> (0.69–1.61 wt%), MgO (0.14–1.14 wt%), and K<sub>2</sub>O (0.02–0.22 wt%) than the core but is relatively  
166 depleted in TiO<sub>2</sub> (<mdl), and V<sub>2</sub>O<sub>5</sub>, (mostly <mdl) and implicitly, also in calculated FeO\*. The darker  
167 domains within the rim (Mag2D) show slightly higher contents of impurities such as Si, Ca, Al, Mg, and  
168 K relative to the brighter domains (Mag2L, [Fig. 5a](#)). In general, elevated contents of impurities reduce  
169 the measured reflectance making such domains darker in both the gamma-enhanced reflected light and  
170 BSE images. These features are further supported by qualitative X-ray mapping of Si, Al, and K  
171 distributions in magnetite ([Fig. 1d–f](#)).

172 Garnet (Fujiashan sample) shows clear textural and compositional variation ([Fig. 2](#)). These garnet  
173 grains are characterized by a well-developed oscillatory zoning texture. The zoning is scarcely visible

174 under reflected light (Fig. 2a, d) but is seen clearly on gamma-enhanced and BSE images (Fig. 2b, c, e,  
175 f). The variation of brightness in gamma-enhanced images corresponds with the change in gray values in  
176 BSE images. EMPA data shows that the garnet of sample FJ279-1 belongs to the grandite series  
177 with >90% andradite + grossular endmembers (Table 2). The brighter domains in gamma-enhanced and  
178 BSE images contain a higher andradite component ( $X_{\text{Adr}} = \sim 91$  to 98, 26.15–29.66 wt% FeO) than the  
179 darker domains ( $X_{\text{Adr}} = \sim 69$  to 81, 21.15–24.35 wt% FeO; Fig. 5b).

180 Although wolframite,  $(\text{Fe},\text{Mn})\text{WO}_4$ , a monoclinic mineral, is suggested to display weak  
181 bireflectance/pleochroism, the reflectance and color of wolframite in the Xingluokeng specimen shows  
182 only faint variation when rotating the microscope stage under plane polarized illumination (Fig. 3a). In  
183 contrast, the gamma-enhanced images show clear differences in brightness between different patchy  
184 zones (Fig. 3b). Two sub-types of domains are recognized according to the change in brightness on the  
185 gamma-enhanced reflected images. Dark domains (Wol1) are observed to be replaced by irregular bright  
186 domains (Wol2). Abundant pores are also found at the boundaries between the two domains. However,  
187 BSE images show only weak difference in gray values even under very high contrast (Fig. 3c). EMPA  
188 data (Table 2) shows that the wolframite in this study features bright domains (Wol2) that have greater  
189 mol.%  $\text{FeWO}_4$  (41.71–62.03) than the dark domains (Wol1, 18.67–42.86  $\text{FeWO}_4$  mol.%; Fig. 5c).  
190 Qualitative X-ray mapping also shows significant differences in Fe and Mn content between these two  
191 domains (Fig. 3d, e).

192 In our case study, the grain margins of tetrahedrite-tennantite are commonly surrounded by  
193 chalcopyrite and pyrite (Fig. 4). Extremely weak variation in reflectance is observed under reflected

194 light with the brighter domains appearing light gray with a brownish tint while the darker domain is  
195 characterized by a greenish-gray tint (Fig. 4a, d). Gamma-enhanced images show these grains have  
196 slightly darker cores (tennantite, Ten) but relatively brighter tetrahedrite rims (Ttr) (Fig. 4b, e), broadly  
197 corresponding to the variation in gray values seen on BSE images (Fig. 4c, f). EMPA data confirm  
198 differences in composition between tennantite (2.55–3.71 atoms per formula unit (apfu) As, 0.08–1.19  
199 apfu Sb) and tetrahedrite (0.41–1.00 apfu As, 2.86–3.61 apfu Sb) (Fig. 5d; Table 4).

### 200 **Green channel intensity and composition profiles**

201 Linear profiles of reflected light green channel intensity were acquired for magnetite and garnet before  
202 and after gamma correction (Fig. 6). The intensity profile across the Mag1 and Mag2 shows only very  
203 small differences prior to gamma correction. However, the Mag2 shows a significant green channel  
204 intensity decrease (10–100) while the average intensity of Mag1 retains a similar intensity following  
205 gamma correction (Fig. 6a). The gamma-enhanced green channel intensity profile also positively  
206 correlates with the variation in Fe content of magnetite but negatively with the total (Si+Ca+Al+Mg)  
207 content (Fig. 6b). The intensity profile across oscillatory zoned garnet shows a relatively small variation  
208 in green channel intensity (40–172) before gamma correction but this expands to 0–238 after gamma  
209 correction (Fig. 6c). The boundaries between individual banded zones are clearly marked by a  
210 fluctuation in intensity. Such a major stretch of green channel intensity enhances differences in  
211 reflectance that reveal grain-scale compositional zonation. The gamma-enhanced green channel intensity  
212 profile is also consistent with the variation of FeO content but negatively correlates with Al<sub>2</sub>O<sub>3</sub> content  
213 (Fig. 6d). Overall, gamma correction significantly stretches the intensity differences between various

214 compositional domains, resulting in notable reflectance differences in the gamma-enhanced images of  
215 both magnetite and garnet.

## 216 **DISCUSSION**

### 217 **Compositional heterogeneity and reflectance variation of Fe-bearing minerals**

218 Magnetite offers, in principle at least, a series of relatively simple substitution possibilities, even though  
219 the mechanisms by which some elements are incorporated are poorly understood or still debated, and  
220 where vacancies in either the Fe or O sites are difficult or impossible to verify directly (Nadoll et al.  
221 2014; Deditius et al. 2018; Ciobanu et al. 2019, 2022). The incorporation of common impurity elements  
222 (mostly Si and Ca in the case considered here, but also others such as Mg, Al and Ti) will decrease both  
223 the reflectance and the average atomic mass of magnetite, as shown in gamma-enhanced images and  
224 BSE images, respectively (Fig. 1a–c). The observations may be readily explained in terms of the  
225 substitution of Si and Ca, and to a lesser extent Al and Mg, for Fe. Iron content is reduced from a mean  
226 of  $23.67 \pm 0.09$  ( $1\sigma$ ,  $n=5$ ) apfu based on a total of 32 oxygen atoms cations in Mag1 to  $22.53 \pm 0.20$  ( $1\sigma$ ,  
227  $n=5$ ) apfu in Mag2L, and just  $21.72 \pm 0.17$  ( $1\sigma$ ,  $n=5$ ) apfu in Mag2D, Fig. 5a; Table 1). This shift  
228 decreases the effective number of free electrons ( $N_{\text{eff}}$ ) expected to re-emit light when excited by incident  
229 light, increasing the energy required to excite electrons into the conduction band and, consequently, a  
230 reduction of reflectance in rim magnetite. This interpretation is further supported by the dataset in the  
231 third edition of Quantitative Data File (QDF3; Criddle and Stanley 1993) showing that Si-rich (2.8 wt%  
232 SiO<sub>2</sub>) magnetite has slightly lower reflectance (~0.7%) than Si-poor magnetite (0.2 wt% SiO<sub>2</sub>) at 589 nm

233 in air. Relative differences in reflectance between Mag1 and Mag2 are also clearly revealed by the green  
234 channel intensity profiles before and after gamma correction (Fig. 6a). It is worth noting that Mag2  
235 contains detectable K<sub>2</sub>O (0.02–0.22 wt%, Table 3), especially in Mag2D (0.11–0.22 wt% K<sub>2</sub>O), whereas  
236 K is absent in Mag1. The strong correlation between K, Al, and Si may indicate the presence of  
237 sub-micron-scale inclusions (phlogopite, for example) contributing to a small decrease in reflectance  
238 (Fig. 1d–f). Recent nanoscale research has documented the presence of sub-micron-sized silicate  
239 inclusions (e.g., diopside, phlogopite, amphibole, and muscovite) in hydrothermal magnetite, a  
240 phenomenon that may be more common than previously thought and could account for aberrant  
241 magnetite compositions (e.g., Deditius et al. 2018; Ciobanu et al. 2019, 2022; Cook et al. 2022). The  
242 presence of sub-micron-sized mineral inclusions may be an additional factor contributing to variation in  
243 reflectance properties in the case considered here.

244 Garnet, a transparent mineral, reveals the relationship between composition and reflectance variation  
245 at the grain scale in our study (Figs. 2, 6c, 6d). Given that Fe has a greater atomic mass than Al, the  
246 relative content of Fe and Al is generally reflected by the gray values seen on BSE images, whereby  
247 brighter domains have higher Fe (andradite component) and darker domains contain more Al (grossular  
248 component) (e.g., Jamtveit et al. 1993; Ciobanu and Cook 2004; Xu et al. 2020). The gamma-enhanced  
249 images (Fig. 2b, e) of Fujiashan garnet show similar variation in brightness as the BSE images (Fig. 2c,  
250 f), readily explained by difference in electron structures between Al<sup>3+</sup> and Fe<sup>3+</sup>, in which Al<sup>3+</sup> has a  
251 larger nucleus and its outermost electrons require higher energy to be excited than is the case for Fe<sup>3+</sup>.  
252 Iron-rich domains in garnet thus have higher reflectance than Al-rich domains and variation in relative

253 brightness simply reflects the relative abundances of Fe<sup>3+</sup> and Al in simple andradite-grossular solid  
254 solutions (Table 2). The green channel intensity profile across compositional domain boundaries can  
255 also be used to reveal variation of Fe<sup>3+</sup> and Al contents at the grain scale (Fig. 6c, d).

256 The name wolframite refers to intermediate members of the wolframite group, a continuous solid  
257 solution between the Fe-rich endmember, ferberite (FeWO<sub>4</sub>), and the Mn-rich end member hübnerite  
258 (MnWO<sub>4</sub>). Wolframite commonly shows compositional heterogeneity (e.g., Campbell and Petersen  
259 1988; Pačevski 2007) with the Mn/Fe ratio exerting primary control on many physical features,  
260 including unit cell dimensions and reflectance (Pačevski 2007). Although reflectance variations are  
261 commonly subtle, they can be observed in gamma-enhanced reflected light images (Fig. 3a, b). Burns  
262 and Vaughan (1970) noted that Mn<sup>2+</sup> has an electronic configuration with half-filled 3d orbitals, which  
263 leads to reduced covalent bonding and higher-lying Fermi levels than Fe<sup>2+</sup>, causing the reflectance of  
264 MnS and MnS<sub>2</sub> to be lower than for the corresponding iron sulfides (FeS and FeS<sub>2</sub>). This phenomenon is  
265 consistent with our observation of wolframite, in which Fe-rich domains are brighter than the Mn-rich  
266 domains in gamma-enhanced reflected light images (Fig. 3b), even when high-contrast BSE images do  
267 not reveal differences in grey values between different domains (Fig. 3c). This is due to the similar mean  
268 atomic mass for FeWO<sub>4</sub>- and MnWO<sub>4</sub>-rich domains (Neiva 2008). The observation emphasizes how  
269 gamma correction can represent a more effective method than BSE imaging to discern compositional  
270 variation among domains with only small mean atomic mass differences in certain minerals.

271 Substituting elements in minerals of the tetrahedrite group, A<sub>6</sub>(B<sub>4</sub>C<sub>2</sub>)D<sub>4</sub>S<sub>13</sub> (Biagioni et al. 2020) may  
272 modify the d electrons in the chemical bonding, resulting in reflectance changes (Hall et al. 1974;

273 [Charlat and Lévy 1976](#)). Changes in Ag occupancy in the A and B sites, substituting for Cu, and  
274 changing Fe/Zn ratios in the C site would lead to a slight increase in the reflectance whereas substitution  
275 of As by Sb in the D site is expected to cause a stronger increase. The significant variation of reflectance  
276 related to the D site is attributed to the covalent character of Sb being stronger than As ([Hall et al. 1974](#)).  
277 Substitution of As by Sb would delocalize electrons, resulting in increasing  $N_{\text{eff}}$  and reflectance.  
278 Differences in the reflectance of tetrahedrite-tennantite cores and rims in our gamma-enhanced images  
279 are broadly comparable with the changes in gray shades seen on the BSE images ([Fig. 4b–f](#)). The darker  
280 core shows higher contents of As and Cu but is relatively depleted in Sb ([Table 4](#); [Fig. 5d](#)). A plausible  
281 explanation for this is the reflectance decrease induced by substitution of As for Sb overwhelms any  
282 increase caused by the change in proportions of Fe and Zn ([Hall et al. 1974](#); [Charlat and Lévy 1976](#)).  
283 The example of tetrahedrite-tennantite illustrates the complexity introduced by minerals in which  
284 multiple substitutions may occur simultaneously in distinct sites and thus masking the relationship  
285 between reflectance variation and composition. To this end, greater attention should be paid to the major  
286 substitution when linking reflectance variation with compositional change in minerals and mineral  
287 groups with complex substitution relationships.

## 288 **Towards a higher reflectance for Fe-rich domains of common Fe-bearing minerals**

289 The minerals in this study have Fe contents ranging from ~1.7 wt% (tetrahedrite-tennantite), through ~7  
290 wt% (wolframite) and ~19 wt% (garnet), to ~69 wt% (magnetite). All show higher reflectance in Fe-rich  
291 domains except for tetrahedrite-tennantite, where Group VA elements (e.g., As and Sb) overwhelmingly  
292 determine changes in reflectance behavior ([Fig. 5](#)). The reflectance of chromite has been suggested to

293 increase with increasing Fe<sup>3+</sup> content (Eales 1980; López-Benito et al. 2017). Awadh (2009) noted that  
294 the reflectance of Fe-rich (16.96 wt% Fe) sphalerite is slightly higher (~0.9 %) than that of Fe-poor  
295 (4.59 wt% Fe) sphalerite at 546 nm in air. Similar results are suggested by recent research on the  
296 reflectance of sphalerite (Lai et al. 2023). The reflectance of pyrite was observed to decrease  
297 systematically with increasing Ni and/or Co concentrations (Vaughan 1969). Recent research on pyrite  
298 shows that unsubstituted Fe-rich domains are brighter than As-rich domains in gamma-enhanced  
299 reflected light images (Zhu et al. 2021). In the case of goethite, FeO(OH), Donskoi et al. (2022) noted  
300 that varieties rich in Al and/or Si have lower reflectance than those with little or no Al and/or Si. It  
301 would therefore appear that Fe-rich domains/grains have higher reflectance in many Fe-bearing minerals  
302 (Table 5). This phenomenon is best explained by the difference in electronic structure between Fe ion  
303 (Fe<sup>2+</sup>, Fe<sup>3+</sup>) and other common constituents (transition metals (Co<sup>2+</sup>, Ni<sup>2+</sup>, Mn<sup>2+</sup>, and Zn<sup>2+</sup>),  
304 alkaline-earth metals (Mg<sup>2+</sup> and Ca<sup>2+</sup>), semimetals (Si<sup>4+</sup> and As<sup>3+</sup> or As<sup>-</sup>), and Al<sup>3+</sup>). The Fe ion has  
305 stronger covalent bonding and delocalization of excited t<sub>2g</sub> electrons than that of the abovementioned  
306 elements, resulting in a larger value of the effective number of free electrons that can be excited to  
307 re-emit light when visible light is incident on their surface, and hence higher reflectance (Vaughan 1969;  
308 Burns and Vaughan 1970). This rule can however be challenged whenever simultaneous substitutions of  
309 multiple elements take place, causing divergent changes in reflectance and leading to a mixed or  
310 averaged-out result. This is particularly true when Fe is a relatively low-concentration constituent, as in  
311 tetrahedrite-tennantite (Fig. 5d).



312

## IMPLICATIONS FOR MINERAL CHARACTERIZATION

313 Previous research has suggested that the reflectance of minerals may be affected by internal factors such  
314 as chemical composition, crystal orientation (anisotropic mineral), and the presence of tiny inclusions as  
315 well as external factors including quality of the polished surface, surface tarnishing, grain size (too-small  
316 grain will induce errors), light wavelength, immersion medium (air or oil), and the instrumentation and  
317 set-up conditions for quantitative measurement (e.g., [Criddle 1990](#); [Criddle and Stanley 1993](#); [Craig and](#)  
318 [Vaughan 1994](#)). Among these, chemical composition and crystal orientation (in anisotropic minerals)  
319 may contribute to significant reflectance variation although their interrelationships and the reflectance of  
320 many minerals remains unclear or inadequately constrained (e.g., [Criddle and Stanley 1993](#); [Craig and](#)  
321 [Vaughan 1994](#)). The gamma correction method is expected to enhance subtle grain-scale variation in  
322 reflectance under reflected light, caused by compositional variation, of Fe-bearing minerals ([Figs. 1–4](#)).  
323 This method is readily achieved using an optical microscope and digital image processing function of  
324 certain software, without destroying the mineral surface and is moreover reproducible, thus representing  
325 a significant advantage over traditional chemical etching and staining techniques ([Ramdohr 1969](#); [Fleet](#)  
326 [et al. 1993](#); [Craig 2001](#); [Gregory et al. 2019](#)). Our study demonstrates that gamma correction is a rapid  
327 and valid tool for assessing compositional heterogeneity of not only the opaque minerals (magnetite,  
328 wolframite, and tetrahedrite-tennantite; [Figs. 1, 3, 4](#)) but also transparent minerals such as garnet ([Fig. 2](#))  
329 with reflectance as low as ~9 % at 589 nm in air ([Criddle 1998](#)). Although internal fractures or crystal  
330 defects induce internal reflections that cause color interference and mask some features during gamma  
331 correction ([Fig. 2b, e](#)), application of the method on (semi-) transparent minerals provides an alternative

17

332 way to constrain composition variation on epoxy-mounted polished blocks. This type of sample is  
333 widely used for quantification of trace element concentration by laser ablation inductively coupled  
334 plasma mass spectrometry (LA-ICP-MS) but cannot be observed under transmitted light. The enhanced  
335 variation of reflectance for transparent minerals is, however, smaller than that of opaque minerals when  
336 using the same gamma values. Prior work also suggested that gamma-enhanced reflected light images  
337 can provide sufficient contrast to differentiate crystal boundaries in marcasite (Fig. 3a, b in [Zhu et al.](#)  
338 [2021](#)). However, the pronounced weak bireflectance for wolframite was insignificant within grains in  
339 our study. Variation in reflectance variation induced by composition appeared more significant than by  
340 crystallographic orientation. To this extent, the gamma correction method has the potential to assist  
341 segmentation and characterization of specific anisotropic minerals with subtle reflectance variation,  
342 without requiring stage rotation, use of crossed polars, or the quarter-wave plate (e.g., for hematite;  
343 [Gomes et al. 2013](#); [Iglesias et al. 2018](#)). A plausible strategy for anisotropic minerals with strong  
344 bireflectance is to compare grains with, or rotate the stage of the optical microscope to, a specific  
345 crystallographic orientation to minimize the influence of reflectance by crystallographic orientation.  
346 Gamma correction may still be useful for constraining the compositional heterogeneity of anisotropic  
347 minerals under such a prerequisite or using sections with specific crystallographic orientations.

348 Gamma-enhanced variation in the relative reflectance can be either the same as (e.g.,  
349 tetrahedrite-tennantite, garnet, and magnetite), or contrasting with (e.g., pyrite, [Zhu et al. 2021](#)), the  
350 change in gray values seen on BSE images, which vary as a function of mean atomic mass ([Paterson et](#)  
351 [al. 1989](#); [Craig et al. 1998](#); [Craig 2001](#)). These relationships represent an implicit link between

352 reflectance variation and compositional variation. The intensity profile of the signal light channel in the  
353 gamma-enhanced reflected light image is thus directly comparable to the composition profile although it  
354 is an aggregated response to the increase and decrease of reflectance caused by individual element  
355 substitutions and/or sub-micron-sized mineral inclusions (Fig. 6). Given that multiple elements are  
356 commonly located in the same crystal sites in many complex solid solution series (e.g., spinel, garnet,  
357 tetrahedrite-tennantite), reflectance variation in the gamma-enhanced image is a cumulative effect  
358 reflecting the change in the average effective number of free electrons of the mineral surface. The  
359 substitution-induced Fe-rich domains are expected to have higher reflectance than Fe-poor domains  
360 whenever Fe is a major constituent (Fig. 5a–c). The gamma-enhanced images of certain minerals may be  
361 more perspicuous than the respective BSE images whenever the differences in atomic mass between  
362 substituted and substituting elements is too small to cause significant gray value variation (e.g., Mn for  
363 Fe in wolframite, Co and/or Ni for Fe in pyrite; Fig. 3b, c; Vaughan 1969; Craig et al. 1998). Further  
364 applications are thus expected to be found in mineral/porosity segmentation and texture classification,  
365 which are of fundamental importance in automated and quantitative optical mineral characterization. It  
366 could be used, for example, to address other economically important iron-oxides and hydroxides (e.g.,  
367 goethite, hematite, magnetite) that have complex, varying chemical compositions that cannot be reliably  
368 constrained by SEM-EDS and other traditional methods alone (Iglesias et al. 2018; López-Benito et al.  
369 2020; Donskoi et al. 2022). These minerals and the porosity between their particles are expected to  
370 display marked differences in gray levels and therefore easy to identify and segment automatically if the  
371 gamma value and acquisition conditions are kept stable (Iglesias et al. 2018; Donskoi et al. 2022). The

372 reproducibility of this process is one key advantage of using automatic acquisition in preference to a  
373 human operator (Iglesias et al. 2018). Recent research has highlighted the potential of coupled  
374 cathodoluminescence (CL) spectra and SEM for characterizing the mineralogy, chemical composition,  
375 and crystal properties of goethite, hematite, and magnetite (Galili et al. 2023). This no-destructive  
376 method relies on the SEM instrument to locate target minerals and is strongly challenged by the  
377 interface of nearby high-luminescence minerals (e.g., quartz and carbonate minerals). Gamma correction  
378 is low-cost and easy to conduct although it lacks a comparable range of magnification and spatial  
379 resolution. Gamma correction nevertheless represents an alternative, optical-based technique that can be  
380 used instead of or complement BSE imaging.

381 In general, gamma correction can be used as a routine method to assess compositional heterogeneity  
382 for certain Fe-bearing opaque and even transparent minerals prior to quantitative analysis. It can also  
383 provide robust textural evidence for minerals that have undergone multiple stages of overgrowth or  
384 display variations in growth habit from core to rim, in turn indicating an evolution of hydrothermal fluid  
385 or magma (e.g., Murowchick and Barnes 1987; Craig 2001; Ciobanu and Cook 2004). Gamma  
386 correction may therefore open a broad range of innovative applications in (automated) mineral  
387 characterization, mineral exploration, and metal recovery.

#### 388 ACKNOWLEDGEMENTS

389 We acknowledge Drs. Zhenyu Chen and Xiaodan Chen (Institute of Mineral Resources, CAGS) for assistance  
390 with scanning electron microscope operation and electron probe microanalysis. Special thanks are due to Senior  
391 Engineers Qingyue Hu, Shanggang Jin, and Ketao Wei (First Geological Team of Hubei Geological Bureau), and

392 Dr. Yunhao Ji (CUGB) for assistance with fieldwork and sample collection. This research was funded by the  
393 National Natural Science Foundation of China (41925011, 92162217), and Basic Scientific Research Operation  
394 Cost of State-Leveled Public Welfare Scientific Research Courtyard (KK2212). Two reviewers and Associate  
395 Editor Callum Hetherington are thanked for their valuable comments on our work that helped us improve clarity.

## 396 REFERENCES CITED

- 397 Abraitis, P.K., Pattrick, R.A.D., and Vaughan, D.J. (2004) Variations in the compositional, textural and electrical  
398 properties of natural pyrite: A review. *International Journal of Mineral Processing*, 74, 41–59.
- 399 Awadh, S.M. (2009) Iron content variations in sphalerite and their effects on reflectance and internal reflections  
400 under reflected light. *Arabian Journal of Geosciences*, 2, 139–142.
- 401 Babedi, L., Von Der Heyden, B.P., Neethling, P.H., and Tadie, M. (2019) The effect of Cd-substitution on the  
402 Raman vibrational characteristics of sphalerite. *Vibrational Spectroscopy*, 105, 102968.
- 403 Berkh, K., and Rammlmair, D. (2022) The effect of Co substitution on the Raman spectra of pyrite: potential as an  
404 assaying tool. *European Journal of Mineralogy*, 34, 259–274.
- 405 Biagioni, C., George, L. L., Cook, N. J., Makovicky, E., Moëlo, Y., Pasero, M., Sejkora, J., Stanley, C.J., Welch,  
406 M.D., and Bosi, F. (2020) The tetrahedrite group: Nomenclature and classification. *American Mineralogist*,  
407 105, 109–122.
- 408 Burns, R.G., and Vaughan, D.J. (1970) Interpretation of the reflectivity behavior of ore minerals. *American*  
409 *Mineralogist*, 55, 1576–1586.
- 410 Buzatu, A., Buzgar, N., Damian, G., Vasilache, V., and Apopei, A.I. (2013) The determination of the Fe content in  
411 natural sphalerites by means of Raman spectroscopy. *Vibrational Spectroscopy*, 68, 220–224.

- 412 Campbell, A., and Petersen, U. (1988) Chemical zoning in wolframite from San Cristobal, Peru. *Mineralium*  
413 *Deposita*, 23, 132–137.
- 414 Cervelle, B., Levy, C., and Caye, R. (1971) Dosage rapide du magnésium dans les ilménites par  
415 microréfectométrie. *Mineralium Deposita*, 6, 34–40.
- 416 Charlat, M., and Lévy, C. (1976) Influence des principales substitutions sur les propriétés optiques dans la série  
417 tennantite-tétraédrite. *Bull. Soc. française Minéral. Cristallograph*, 99, 29–37.
- 418 Ciobanu, C. L., Verdugo-Ihl, M. R., Cook, N. J., Ehrig, K., Slattery, A., and Courtney-Davies, L. (2022).  
419 Ferro-tschermakite with polysomatic chain-width disorder identified in silician magnetite from Wirrda Well,  
420 South Australia: A HAADF STEM study. *American Mineralogist*, 107, 765–777.
- 421 Ciobanu, C.L., and Cook, N.J. (2004) Skarn textures and a case study: the Ocna de Fier-Dognecea orefield, Banat,  
422 Romania. *Ore Geology Reviews*, 24, 315–370.
- 423 Ciobanu, C.L., Verdugo-Ihl, M.R., Slattery, A., Cook, N.J., Ehrig, K., Courtney-Davies, L., and Wade, B.P. (2019)  
424 Silician magnetite: Si–Fe–Nanoprecipitates and other mineral inclusions in magnetite from the Olympic Dam  
425 deposit, South Australia. *Minerals*, 9, 311.
- 426 Cook, N.J., Ciobanu, C.L., Ehrig, K., Slattery, A.D., and Gilbert, S.E. (2022) Micron- to atomic-scale  
427 investigation of rare earth elements in iron oxides. *Frontiers in Earth Science*, 10, 967189.
- 428 Cook, N.J, Ciobanu, C.L., George, L., Zhu, Z.Y., Wade, B., and Ehrig, K. (2016) Trace element analysis of  
429 minerals in magmatic-hydrothermal ores by laser ablation inductively-coupled plasma mass spectrometry:  
430 Approaches and opportunities. *Minerals*, 6, 111.
- 431 Craig, J.R., (2001) Ore-mineral textures and the tales they tell. *The Canadian Mineralogist*, 39, 937–956.

- 432 Craig, J.R., and Vaughan, D.J. (1994) *Ore Microscopy and Ore Petrography*, 2nd ed., 434 p. John Wiley and Sons,  
433 Inc., New York.
- 434 Craig, J.R., Vokes, F.M., and Solberg, T.N. (1998) Pyrite: Physical and chemical textures. *Mineralium Deposita*,  
435 34, 82–101.
- 436 Criddle, A. J., Jambor, J. L., and Vaughan, D. J. (1990) Microscope-photometry, reflectance measurement, and  
437 quantitative color. In: J.L. Jambor and D.J. Vaughan, Eds., *Advanced Microscopic Studies of Ore Minerals*, 17,  
438 135–169.
- 439 Criddle, A.J. (1998) Ore microscopy and photometry (1890–1998). In: L. Cabri and D.J. Vaughan, Eds., *Modern*  
440 *Approaches to Ore and Environmental Mineralogy*, 27, 1–74.
- 441 Criddle, A.J., and Stanley, C.J. (1993) *Quantitative Data File for Ore Minerals*, 3<sup>rd</sup> ed., 635 p. Chapman and Hall /  
442 Natural History Museum, London.
- 443 Deditius, A.P., Reich, M., Simon, A.C., Suvorova, A., Knipping, J., Roberts, M.P., Rubanov, S., Dodd, A., and  
444 Saunders, M. (2018) Nanogeochemistry of hydrothermal magnetite. *Contributions to Mineralogy and*  
445 *Petrology*, 173, 46.
- 446 Ding, L.X., Huang, G.C., and Xia, J.L. (2014) Petrogenesis of the Longjiaoshan-Fujiashan porphyritic intrusion in  
447 southeastern Hubei Province and implications for Cu-W mineralization. *Acta Geologica Sinica*, 88, 1513–1527  
448 (in Chinese with English abstract).
- 449 Donskoi, E., Manuel, J. R., Hapugoda, S., Poliakov, A., Raynlyn, T., Austin, P., and Peterson, M. (2022)  
450 Automated optical image analysis of goethitic iron ores. *Mineral Processing and Extractive Metallurgy*, 131,  
451 14–24.

- 452 Eales, H.V. (1980) The application of reflectivity measurements to the study of chromiferous spinels. The  
453 Canadian Mineralogist, 18, 17–23.
- 454 Fleet, M.E., Chryssoulis, S.L., MacLean, P.J., Davidson, R. and Weisener, C.G. (1993) Arsenian pyrite from gold  
455 deposits; Au and As distribution investigated by SIMS and EMP, and color staining and surface oxidation by  
456 XPS and LIMS. The Canadian Mineralogist, 31, 1–17.
- 457 Galili, N., Kaplan-Ashiri, I., and Halevy, I. (2023) Cathodoluminescence of iron oxides and oxyhydroxides.  
458 American Mineralogist, 108, 1436–1448.
- 459 George, L.L., Biagioni, C., D’Orazio, M., and Cook, N.J. (2018) Textural and trace element evolution of pyrite  
460 during greenschist facies metamorphic recrystallization in the southern Apuan Alps (Tuscany, Italy): Influence  
461 on the formation of Tl-rich sulfosalt melt. Ore Geology Reviews, 102, 59–105.
- 462 George, L.L., Biagioni, C., Lepore, G.O., Lacalamita, M., Agrosi, G., Capitani, G.C., Bonaccorsi, E., and  
463 d’Acapito, F. (2019) The speciation of thallium in (Tl, Sb, As)-rich pyrite. Ore Geology Reviews, 107, 364–  
464 380.
- 465 Gomes, O.D.M., Iglesias, J.C.A., Paciornik, S., and Vieira, M.B. (2013) Classification of hematite types in iron  
466 ores through circularly polarized light microscopy and image analysis. Minerals Engineering, 52, 191–197.
- 467 Gregory, D.D., Large, R.R., Bath, A.B., Steadman, J.A., Wu, S., Danyushevsky, L., Bull, S.W., Holden, P., and  
468 Ireland, T.R. (2016) Trace element content of pyrite from the Kapaï Slate, St. Ives Gold District, Western  
469 Australia. Economic Geology, 111, 1297–1320.
- 470 Gregory, D.D., Mukherjee, I., Olson, S.L., Large, R.R., Danyushevsky, L.V., Stepanov, A.S., Avila, J.N., Cliff, J.,  
471 Ireland, T.R., Raiswell, R., and others (2019) The formation mechanisms of sedimentary pyrite nodules



- 472 determined by trace element and sulfur isotope microanalysis. *Geochimica et Cosmochimica Acta*, 259, 53–68.
- 473 Guo, X.Z., Zhou, T.F., Wang, F.Y., Ye, S.Z., and Feng, D.S. (2021) Study of occurrence states and precipitation  
474 mechanism of tellurium in Chengmenshan porphyry-skarn deposit from the Middle-Lower Yangtze River  
475 Valley Metallogenic Belt. *Acta Petrologica Sinica*, 37, 2723–2742 (in Chinese with English abstract).
- 476 Hall, A.J., Cervelle, B., Lévy, C. (1974) The effect of substitution of Cu by Zn, Fe and Ag on the optical  
477 properties of synthetic tetrahedrite,  $\text{Cu}_{12}\text{Sb}_4\text{S}_{13}$ . *Bulletin de Minéralogie*, 97, 18–26.
- 478 Iglesias, J.C.Á., Augusto, K.S., Gomes, O.D.F.M., Domingues, A.L.A., Vieira, M.B., Casagrande, C., and  
479 Paciornik, S. (2018) Automatic characterization of iron ore by digital microscopy and image analysis. *Journal*  
480 *of Materials Research and Technology*, 7, 376–380.
- 481 Jamtveit, B., Wogelius, R.A., and Fraser, D.G. (1993) Zonation patterns of skarn garnets: Records of  
482 hydrothermal system evolution. *Geology*, 21, 113–116.
- 483 Jehlička, J., and Culka, A. (2022) Critical evaluation of portable Raman spectrometers: From rock outcrops and  
484 planetary analogs to cultural heritage—A review. *Analytica Chimica Acta*, 1209, 339027.
- 485 Ji, Y.H., Xie, G.Q., Zhu, Q.Q., Sun, X.F., and Li, X.H. (2019) Influence of carbonaceous strata on skarn tungsten  
486 deposits: A case study of Fujiashan deposit in eastern Hubei Province. *Mineral Deposits*, 38, 917–934 (in  
487 Chinese with English abstract).
- 488 Lai, X., Chen, C.H., Yang, Y.L., Liu, S.Y., Li, Y., Wang, J.X., Song, Z.J., Gu, Y., Chen, X.J., and Huang, X.D.  
489 (2023) Constraints on Metallogenic Temperature and Mineralization Style from Reflection Color of Sphalerite.  
490 *Ore Geology Reviews*, 161, 105634.
- 491 López-Benito, A., Catalina, J. C., Alarcón, D., Grunwald, Ú., Romero, P., and Castroviejo, R. (2020). Automated

- 492 ore microscopy based on multispectral measurements of specular reflectance. I—A comparative study of some  
493 supervised classification techniques. *Minerals Engineering*, 146, 106136.
- 494 López-Benito, A., Gervilla, F., Catalina, J.C., and Castroviejo, R. (2017) Chromite typology and composition  
495 characterized through multispectral specular reflectance. *Ore Geology Reviews*, 89, 132–142.
- 496 Murowchick, J.B., and Barnes, H.L. (1987) Effects of temperature and degree of supersaturation on pyrite  
497 morphology. *American Mineralogist*, 72, 1241–1250.
- 498 Nadoll, P., Angerer, T., Mauk, J.L., French, D., and Walshe, J. (2014) The chemistry of hydrothermal magnetite: a  
499 review. *Ore Geology Reviews*, 61, 1–32.
- 500 Neiva, A. (2008) Geochemistry of cassiterite and wolframite from tin and tungsten quartz veins in Portugal. *Ore*  
501 *Geology Reviews*, 33, 221–238.
- 502 Pačevski, A., Götzinger, M., Dimitrijević, R. and Cvetković, L. (2007) Oscillatory zoning in wolframite from  
503 Osanica, near Bor, Serbia. *Neues Jahrbuch für Mineralogie-Abhandlungen, Journal of Mineralogy and*  
504 *Geochemistry*, 184, 151–160.
- 505 Paterson, B.A., Stephens, W.E., and Herd, D.A. (1989) Zoning in granitoid accessory minerals as revealed by  
506 backscattered electron imagery. *Mineralogical Magazine*, 53, 55–61.
- 507 Ramdohr, P. (1969) *The Ore Minerals and Their Intergrowths*, 1st ed., 1174 p. Pergamon Press, London.
- 508 Saager, R., and Mihalik, P. (1967) Two varieties of pyrite from the Basal Reef of the Witwatersrand System.  
509 *Economic Geology*, 62, 719–731.
- 510 Stanley, C.J. (2013) Quantitative reflected light microscopy: A searchable web-based database of the four COM  
511 wavelengths. <https://www.mindat.org/article.php/1829/Quantitative+reflected+light+microscopy%>

- 512 3A+A+searchable+web-based+database+of+the+ (accessed Jan 9, 2024).
- 513 Tarkian, M. (1987) Compositional variations and reflectance of the common platinum-group minerals.  
514 Mineralogy and Petrology, 36, 169–190.
- 515 Vaughan, D.J. (1969) Zonal variation in bravoite. American Mineralogist, 54, 1075–1083.
- 516 Vaughan, D.J. (1978) The interpretation and prediction of the properties of opaque minerals from crystal chemical  
517 models. Bulletin de Minéralogie, 101, 484–497.
- 518 Wang, H, Feng, C.Y, Li, R.X., Li, C., Zhao, C., Chen, X., and Wang, G.H. (2021b) Ore-forming mechanism and  
519 fluid evolution processes of the Xingluokeng tungsten deposit, western Fujian Province: Constraints from  
520 in-situ trace elemental and Sr isotopic analyses of scheelite. Acta Petrologica Sinica, 37, 698–716 (in Chinese  
521 with English abstract).
- 522 Wang, H., Feng, C.Y., Li, R.X., Zhao, C., Liu, P., Wang, G.H., and Hao, Y.J. (2021a) Petrogenesis of the  
523 Xingluokeng W-bearing granitic stock, western Fujian Province, SE China and its genetic link to W  
524 mineralization. Ore Geology Reviews, 132, 103987.
- 525 Xu, J., Ciobanu, C.L., Cook, N.J., Zheng, Y.Y., Sun, X., and Wade, B.P. (2016) Skarn formation and trace  
526 elements in garnet and associated minerals from Zhibula copper deposit, Gangdese Belt, southern Tibet. Lithos,  
527 262, 213–231.
- 528 Xu, Y.M., Jiang, S.Y., and Zhu, J.X. (2021) Factors controlling the formation of large porphyry Cu deposits: A  
529 case study from the Jiurui ore district of Middle-Lower Yangtze River Metallogenic Belt using in situ zircon  
530 and apatite chemistry from syn-mineralization intrusions. Ore Geology Reviews, 133, 104082.
- 531 Zhu Q.Q., Xie G.Q., and Li W. (2019) Superposition mechanism of Fe enrichment in skarn deposits of Edong

532 district: Constrains from magnetite texture and ore grade data. *Acta Petrologica Sinica*, 35, 3703–3720 (in  
533 Chinese with English abstract).

534 Zhu, Q.Q., Cook, N. J., Xie, G.Q., Ciobanu, C. L., Gilbert, S. E., Wade, B., and Xu, J. (2022) Textural and  
535 geochemical analysis of celestine and sulfides constrain Sr-(Pb-Zn) mineralization in the Shizilishan deposit,  
536 eastern China. *Ore Geology Reviews*, 144, 104814.

537 Zhu, Q.Q., Cook, N.J., Xie, G.Q., Ciobanu, C.L., Jian, W., Wade, B.P., and Xu, J. (2021) Gamma-enhancement of  
538 reflected light images: A rapid, effective tool for assessment of compositional heterogeneity in pyrite.  
539 *American Mineralogist*, 106, 497–505.

540 Zhu, Q.Q., Cook, N.J., Xie, G.Q., Ciobanu, C.L., and Ji Y.H. (2023) Determination of skarn garnet compositions  
541 using Raman spectroscopy. *Journal of Raman Spectroscopy*. 54, 217–224.

542 Zhu, Q.Q., Cook, N.J., Xie, G.Q., Wade, B.P., and Ciobanu, C.L. (2020) Arsenic-induced downshift of Raman  
543 band positions for pyrite. *Economic Geology*, 115, 1589–1600.

544 Zhu, Q.Q., Xie, G.Q., Mao, J.W., Hou, K.J., Sun, J.F., and Jiang, Z.S. (2017) Formation of the Jinshandian Fe  
545 skarn ore field in the Edong district, eastern China: constraints from U-Pb and  $^{40}\text{Ar}/^{39}\text{Ar}$  geochronology. *Ore*  
546 *Geology Reviews*, 86, 1–20.

#### 547 **Figure captions**

548 **FIGURE 1.** Reflected light (a), gamma-enhanced (b), back-scattered electron (BSE) images (c), and qualitative  
549 X-ray element maps (d, e, and f) showing textures and compositional heterogeneity in magnetite (Mag) from  
550 the Jinshandian deposit. Rounded Mag1 (light gray) is preserved as a core domain within Mag2 (gray) as  
551 demonstrated in the reflected light (a), gamma-enhanced (b), and BSE (c) images. The curved boundary

552 between the core domain (Mag1) and rim (Mag2) is marked by white dashed lines in the gamma-enhanced  
553 images (**b**). Boundaries between dark (Mag2D) and bright (Mag2L) domains in the rim are demonstrated in  
554 the gamma-enhanced (marked by white dashed arrow in inset on **b**) and BSE (**c**) images but are only faintly  
555 seen in reflected light (**a**). Compositional heterogeneity in Mag2 and differences between Mag1 and Mag2 are  
556 revealed by variation in the contents of Si (**d**), Al (**e**), and K (**f**).

557 **FIGURE 2.** Reflected light (**a** and **d**), gamma-enhanced (**b** and **e**), and BSE images (**c** and **f**) showing textural and  
558 compositional heterogeneity in andradite-grossular garnet (Grt) from the Fujiashan deposit. Variation in  
559 reflectance of the garnet is hardly visible in reflected light but a clear oscillatory zoning texture is seen on both  
560 gamma-enhanced (**b** and **e**) and BSE images (**c** and **f**). Note the internal fractures or crystal defects induced by  
561 internal reflection may cause color interference and mask some features during gamma correction (marked by  
562 white arrows on **d** and **e**).

563 **FIGURE 3.** Reflected light (**a**), gamma-enhanced (**b**), BSE images (**c**), and qualitative X-ray maps (**d**–**f**) showing  
564 textural and compositional heterogeneity in wolframite (Xingluokeng sample). Reflectance variation in  
565 wolframite (Wol) is hardly visible in reflected light (**a**) and high-contrast BSE images (**c**) but is clearly  
566 demonstrated in the gamma-enhanced image (**b**). Compositional differences between Wol1 and Wol2 are  
567 revealed by variation in the contents of Fe (**d**) and Mn (**e**) while Nb (**f**) shows no difference between the two  
568 domains. Weak brownish internal reflection is shining through and marked by the white arrow in (**a**). The  
569 presence of abundant micro-sized pores near the boundary between Wol1 and Wol2 may indicate replacement  
570 as shown in the gamma-enhanced image (**b**).

571 **FIGURE 4.** Reflected light (**a** and **d**), gamma-enhanced (**b** and **e**), and BSE images (**c** and **f**) showing the texture

572 and compositional heterogeneity of tetrahedrite-tennantite (Chengmenshan sample). Tetrahedrite-tennantite  
573 shows a very weak variation in reflectance and color (from greenish gray to gray with a brownish tint) (**a, b**).  
574 Gamma-enhanced reflected images show clear reflectance variation (**b, e**) and the brightness correlates well  
575 with the gray values of the BSE images (**c, f**). Boundaries between core tennantite (Ten) and rim tetrahedrite  
576 (Ttr) are marked by white dashed lines on the gamma-enhanced images (**b** and **e**). Abbreviations: Ccp–  
577 chalcopryite; Py–pyrite; Ten–tennantite; Ttr–tetrahedrite.

578 **FIGURE 5.** Binary correlation plots from EMPA data showing compositional heterogeneity in magnetite (**a**),  
579 garnet (**b**), wolframite (**c**), and tetrahedrite-tennantite (**d**). Chemical compositions of magnetite and  
580 tetrahedrite-tennantite were calculated based on normalization to 32 O atoms and 29 total atoms, respectively.  
581 Arrows indicate how brightness changes with mineral composition when observed under reflected light.  
582 Abbreviations: Mag–magnetite; Grt–garnet; Wol–wolframite; Ten–tennantite; Ttr–tetrahedrite.

583 **FIGURE 6.** Green channel intensity profiles of reflected light images (**a, c**) and compositional profiles (**b, d**) for  
584 magnetite and garnet at the grain scale. Gray and black lines are intensity profiles before and after gamma  
585 enhancement, respectively.

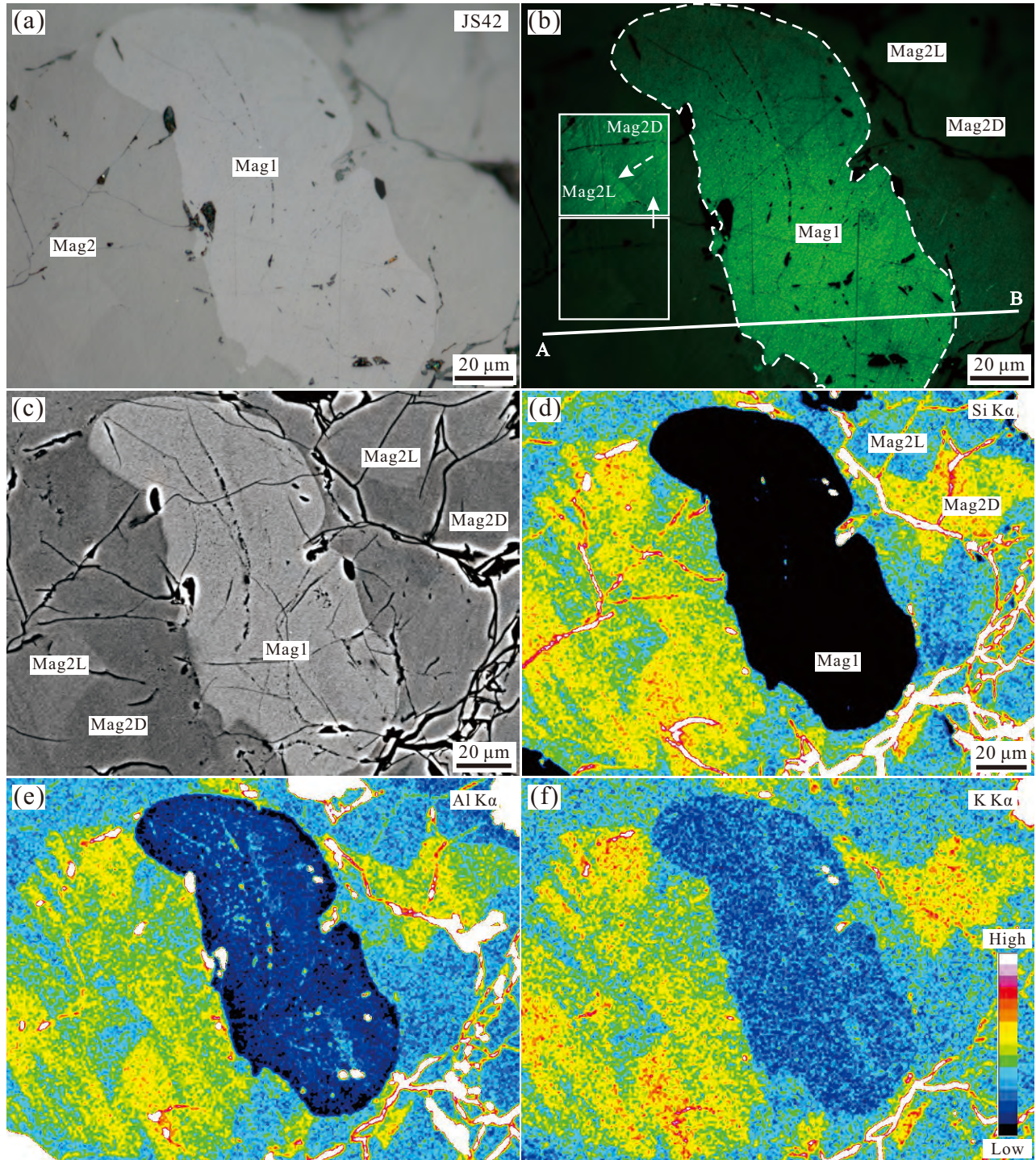


Figure 1

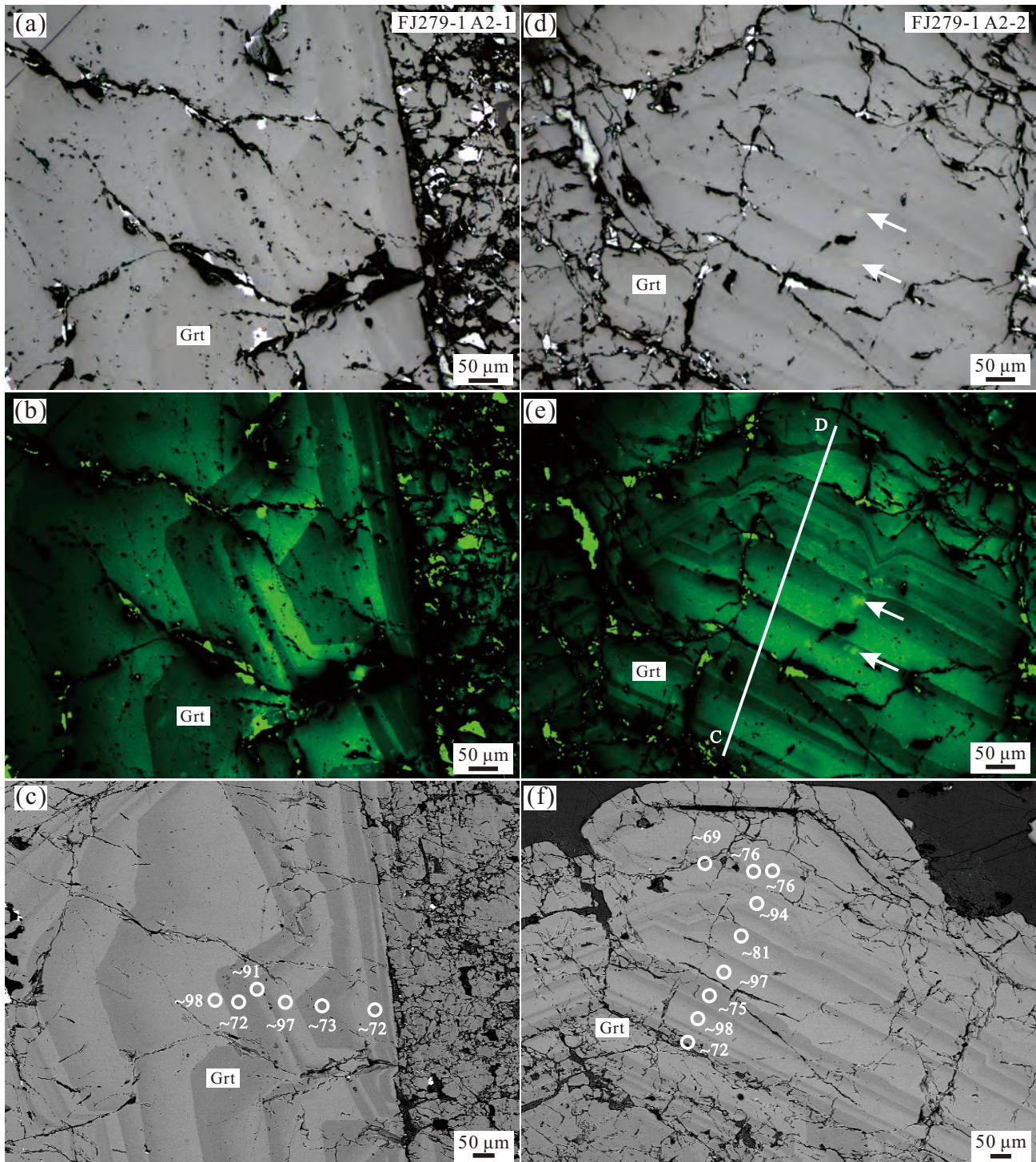


Figure 2



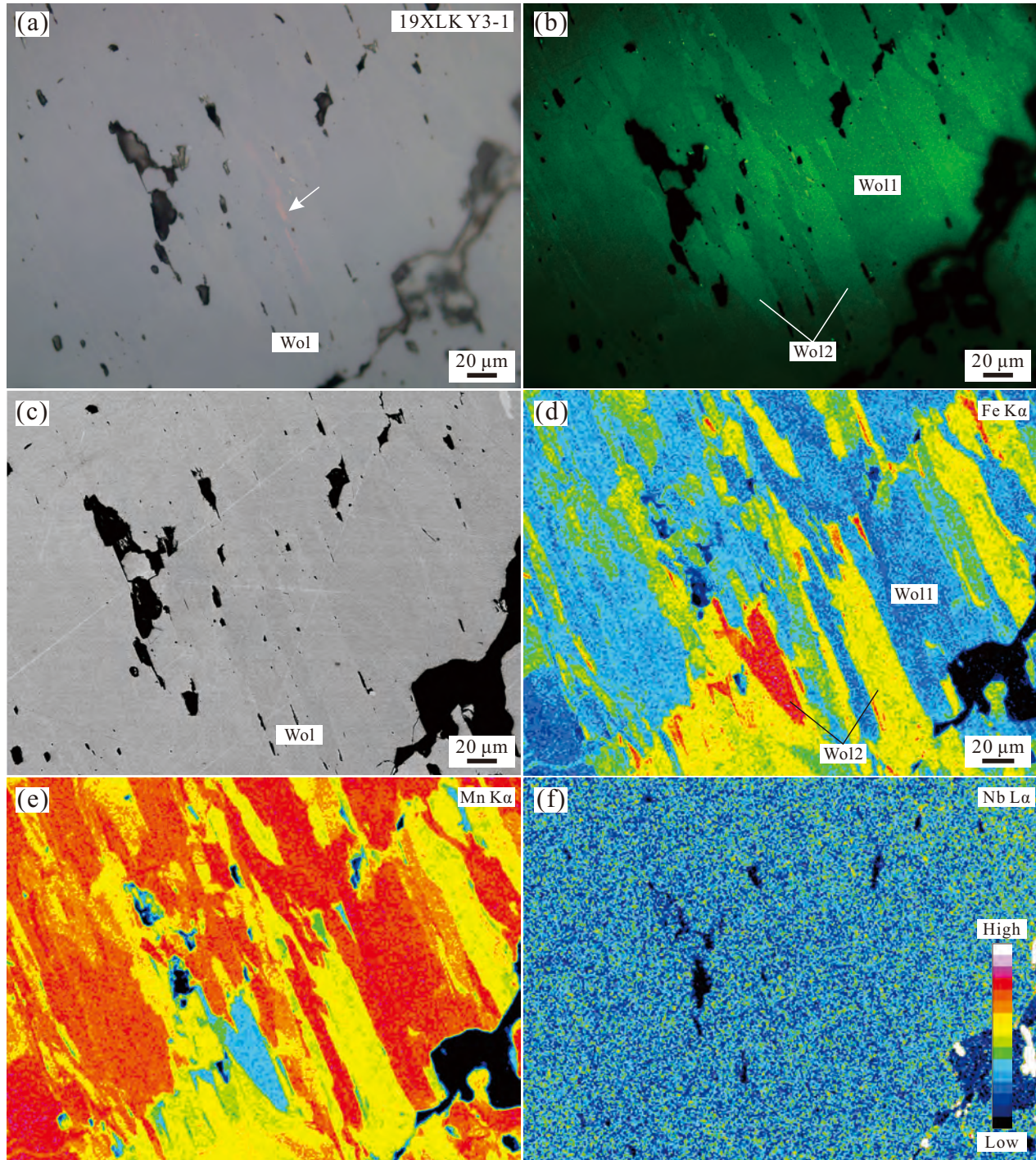


Figure 3

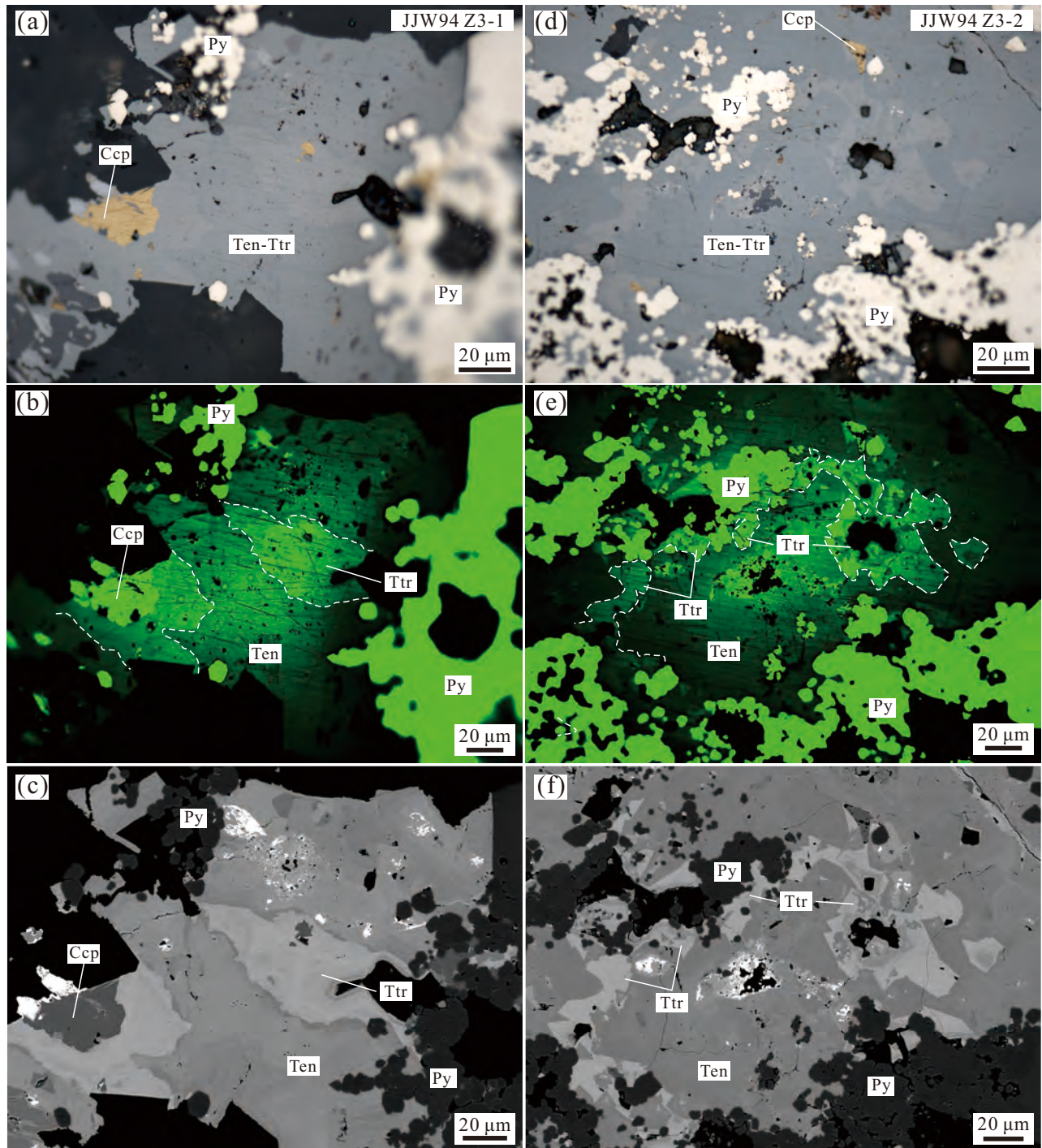


Figure 4

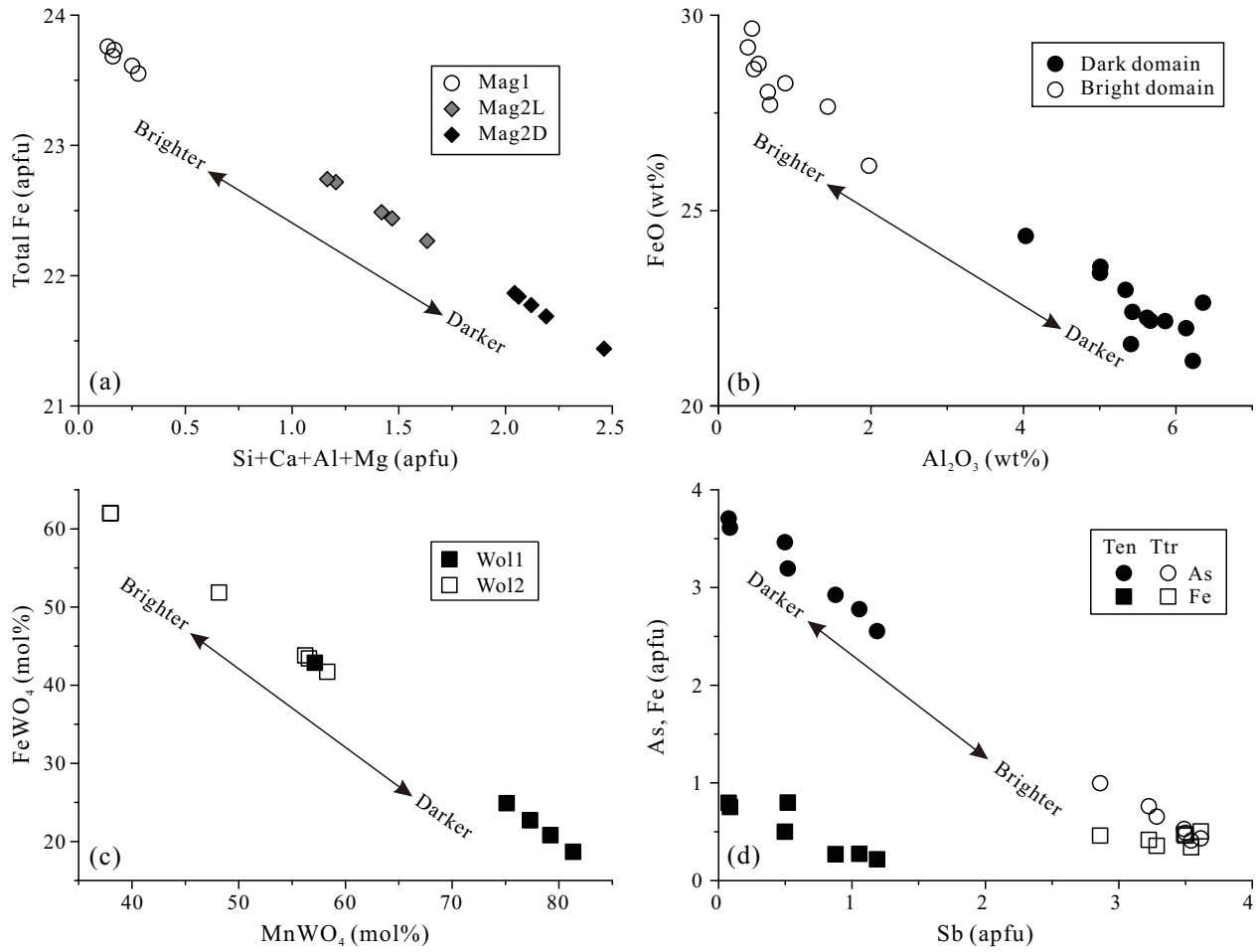


Figure 5

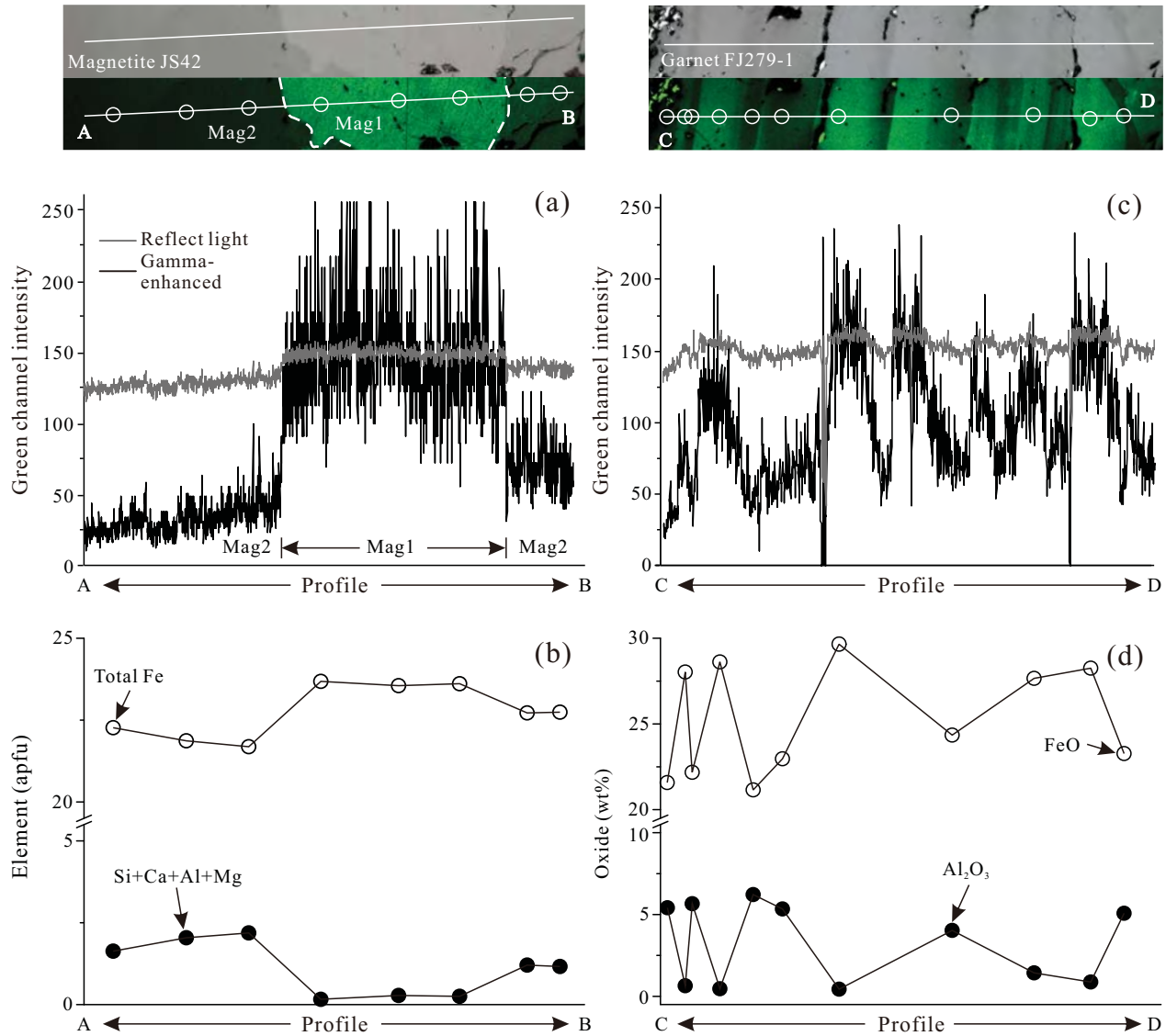


Figure 6

**Table 1.** Electron microprobe data for magnetite (wt%)

Sample	Minimum detection limit	JS42 Y2-3-1										JS42 Z3-1				
		1	2	3	4	5	6	7	8	9	10	1	2	3	4	5
Sub-type		Mag2B	Mag2D	Mag2D	Mag1	Mag1	Mag1	Mag2B	Mag2B	Mag2B	Mag2D	Mag2D	Mag2B	Mag2D	Mag1	Mag1
SiO <sub>2</sub>	0.03	2.52	3.01	2.98	<	<	0.09	1.99	1.97	2.43	3.45	3.43	2.16	3.24	0.05	<
TiO <sub>2</sub>	0.11	<	<	<	0.27	0.27	0.25	<	<	<	<	<	<	<	<	0.12
Al <sub>2</sub> O <sub>3</sub>	0.02	0.98	1.23	1.32	0.30	0.53	0.41	0.69	0.73	0.89	1.45	1.61	0.89	1.34	0.33	0.30
V <sub>2</sub> O <sub>3</sub>	0.03	<	<	0.04	0.09	0.10	0.07	<	<	<	<	<	<	<	<	<
FeO*	0.05	61.20	60.26	60.65	68.49	68.37	68.04	64.38	63.12	62.10	58.96	57.35	62.15	58.94	68.05	68.29
Fe <sub>2</sub> O <sub>3</sub> *		32.10	32.45	32.11	31.09	31.08	31.13	32.48	32.31	32.61	33.53	32.04	32.02	32.87	30.73	30.90
MnO	0.05	0.22	0.18	0.14	0.12	0.17	0.15	0.21	0.15	0.16	0.18	0.10	0.16	0.15	0.13	0.12
MgO	0.03	0.44	0.80	1.14	0.12	0.20	0.16	0.28	0.14	0.23	0.45	1.07	0.34	0.51	0.07	0.06
CaO	0.02	0.95	1.04	1.00	<	<	<	0.74	0.73	0.96	1.14	1.04	0.86	1.13	<	<
CoO	0.04	0.10	0.06	0.14	0.17	0.13	0.08	0.09	0.14	0.13	0.10	0.13	0.10	0.11	0.12	0.09
Na <sub>2</sub> O	0.02	0.10	0.14	0.22	<	0.04	0.03	<	0.13	0.10	0.15	0.15	0.16	0.13	0.07	<
K <sub>2</sub> O	0.01	0.06	0.12	0.11	<	<	0.01	0.02	0.02	0.05	0.14	0.22	0.05	0.15	<	<
Total		98.65	99.28	99.87	100.64	100.89	100.42	100.88	99.44	99.65	99.56	97.12	98.89	98.55	99.54	99.87
Calculated based on 32 oxygen atoms																
Si		0.77	0.91	0.89	0.00	0.00	0.03	0.60	0.60	0.74	1.04	1.05	0.66	0.98	0.02	0.00
Ti		0.00	0.00	0.00	0.06	0.06	0.06	0.00	0.00	0.00	0.00	0.00	0.00	0.00	0.00	0.03
Al		0.35	0.44	0.47	0.11	0.19	0.15	0.24	0.26	0.32	0.51	0.58	0.32	0.48	0.12	0.11
V		0.00	0.00	0.01	0.02	0.03	0.02	0.00	0.00	0.00	0.00	0.00	0.00	0.00	0.03	0.02
Fe <sup>2+</sup>		8.20	8.18	8.03	7.94	7.90	7.96	8.16	8.24	8.27	8.43	8.21	8.19	8.36	7.93	7.95
Fe <sup>3+</sup>		14.07	13.68	13.65	15.74	15.65	15.65	14.56	14.50	14.17	13.34	13.23	14.30	13.48	15.80	15.81
Total Fe		22.27	21.87	21.69	23.68	23.55	23.61	22.72	22.74	22.44	21.77	21.44	22.49	21.84	23.73	23.76
Mn		0.06	0.04	0.04	0.03	0.04	0.04	0.05	0.04	0.04	0.05	0.03	0.04	0.04	0.04	0.03
Mg		0.20	0.36	0.51	0.05	0.09	0.07	0.13	0.06	0.10	0.20	0.49	0.15	0.23	0.03	0.03
Ca		0.31	0.34	0.32	0.00	0.00	0.00	0.24	0.24	0.31	0.37	0.34	0.28	0.37	0.00	0.00
Co		0.02	0.02	0.03	0.04	0.03	0.02	0.02	0.03	0.03	0.02	0.03	0.03	0.03	0.03	0.02
Na		0.01	0.02	0.03	0.00	0.01	0.00	0.00	0.02	0.01	0.02	0.02	0.02	0.02	0.01	0.00
K		0.01	0.01	0.01	0.00	0.00	0.00	0.00	0.00	0.00	0.01	0.02	0.00	0.01	0.00	0.00
Si+Ca+Al+Mg		1.63	2.04	2.19	0.16	0.28	0.25	1.21	1.16	1.47	2.12	2.46	1.42	2.06	0.17	0.14

Notes: Mag—magnetite; <—below minimum limit of detection;  
\* Signifies recalculated values based on 32 oxygen atoms.

**Table 2.** Electron microprobe data for garnet (wt%)

Sample	Minimum detection limit	FJ279-1 A2-1								FJ279-1 A2-2												
		1	2	3	4	5	6	7	8	1	2	3	4	5	6	7	8	9	10	11	12	13
Sub-type		Dark	Bright	Dark	Bright	Dark	Bright	Dark	Bright	Dark	Bright	Dark	Bright	Dark	Dark	Bright	Dark	Bright	Bright	Dark	Dark	Dark
			t		t		t		t		t		t			t		t	t			
SiO <sub>2</sub>	0.03	36.3 3	35.45	36.6 3	35.07	36.0 8	35.01	37.1 2	35.12	36.7 1	35.13	35.8 3	35.19	36.2 2	36.1 3	34.99	36.4 2	35.36	35.53	36.5 1	35.8 5	37.48
TiO <sub>2</sub>	0.03	0.59	0.04	0.40	0.04	0.16	<	0.19	<	0.56	0.03	0.52	<	0.44	0.61	<	<	<	0.04	0.04	0.08	0.04
Al <sub>2</sub> O <sub>3</sub>	0.02	5.86	0.68	5.43	0.53	6.13	1.97	5.62	0.39	5.41	0.65	5.66	0.47	6.22	5.34	0.44	4.03	1.43	0.88	5.01	5.01	6.36
Cr <sub>2</sub> O <sub>3</sub>	0.03	<	<	0.05	<	0.05	<	<	<	0.03	<	<	<	<	<	<	<	<	<	<	<	<
FeO	0.03	22.1 7	27.71	22.4 0	28.75	21.9 9	26.15	22.2 6	29.18	21.5 8	28.03	22.1 8	28.62	21.1 5	22.9 7	29.66	24.3 5	27.66	28.26	23.4 0	23.5 6	22.64
MnO	0.03	0.64	0.44	0.52	0.57	0.63	0.48	0.48	0.45	0.62	0.40	0.49	0.39	0.87	0.57	0.38	0.57	0.41	0.53	0.90	0.89	1.22
MgO	0.02		0.06	0.11	0.04	0.04	0.03	0.05	0.03	0.08	0.08	0.06		0.08	0.05	0.04	0.04					0.04
CaO	0.01	34.0 1	33.41	34.0 7	33.25	34.0 7	33.64	33.8 2	32.82	33.7 0	33.26	33.7 7	33.43	33.4 3	33.5 6	33.29	33.8 1	33.60	32.83	32.9 3	33.0 1	32.58
Na <sub>2</sub> O	0.02	0.02	<	<	<	<	<	<	<	<	<	0.03	<	<	0.02	0.02	<	<	<	<	<	<
Total		99.6 2	97.78	99.6 0	98.25	99.1 5	97.28	99.5 4	97.98	98.6 9	97.58	98.5 4	98.10	98.4 2	99.2 4	98.81	99.2 2	98.47	98.06	98.7 9	98.3 9	100.3 5
End member (mol%)																						
Morimotoite								0.41		0.23											0.23	
Spessartine									1.09	2.75				1.95	1.30				1.25	2.07	0.64	2.75
Almandine									1.63	4.25					0.02				0.04	1.67		4.25
Grossular		24.2 5	1.45	23.0 6		25.0 7	6.48	23.5 9		22.4 9	0.42	22.9 9		25.0 1	20.5 3		17.3 8	3.85	1.26	19.2 2	20.4 4	22.49
Andradite		71.8 8	96.84	73.7 2	97.29	71.6 7	90.93	72.3 0	98.01	68.9 5	97.38	73.5 4	97.75	70.4 4	74.8 1	96.79	80.9 1	93.83	96.16	76.1 8	75.9 2	68.95
Remainder		1.41	1.33	0.74	2.58	2.45	2.45	0.00	1.99	0.88	1.77	1.64	2.25	0.60	1.29	3.21	1.20	2.32	0.93	0.42	1.92	0.88

Notes: <—below minimum limit of detection.

**Table 3.** Electron microprobe data for wolframite (wt%)

Sample	Minimum detection limit	19XLK57 Y4-1					19XLK57 Y3-1					
		1	2	3	4	5	1	2	3	4	5	6
Sub-type		Wol2	Wol1	Wol2	Wol1	Wol2	Wol1	Wol2	Wol1	Wol2	Wol2	Wol1
FeO	0.07	15.25	10.17	14.83	4.99	12.64	5.83	10.24	4.37	9.31	10.50	5.37
MnO	0.07	9.22	13.39	8.97	18.76	11.59	17.36	13.18	18.81	12.85	13.37	18.04
WO <sub>3</sub>	0.10	76.37	76.22	77.14	76.70	77.36	76.75	75.38	76.68	76.83	76.72	77.42
Total		100.84	99.81	100.99	100.46	101.60	99.96	98.82	99.88	99.00	100.62	100.86
Calculated based on 4 oxygen atoms												
Fe		0.64	0.43	0.62	0.21	0.53	0.24	0.43	0.18	0.39	0.44	0.22
Mn		0.39	0.57	0.38	0.80	0.49	0.74	0.56	0.80	0.54	0.57	0.76
W		0.99	0.99	1.00	0.99	1.00	1.00	0.98	0.99	1.00	1.00	1.00
End member (mol%)												
MnWO <sub>4</sub>		37.97	57.14	37.99	79.21	48.15	75.11	56.59	81.33	58.29	56.34	77.30
FeWO <sub>4</sub>		62.03	42.86	62.01	20.79	51.85	24.89	43.41	18.67	41.71	43.66	22.70

Notes: Wol–wolframite.



**Table 4.** Electron microprobe data for tetrahedrite-tennantite (wt%)

Sample	Minimum detection limit	JJW94 Z3-1							JJW94 Z3-2						
		1	2	3	4	5	6	7	1	2	3	4	5	6	7
Sub-type		Ttr	Ttr	Ten	Ten	Ttr	Ttr	Ten	Ten	Ttr	Ten	Ttr	Ten	Ten	Ttr
As	0.03	1.86	3.50	13.51	12.28	2.99	2.22	14.46	18.20	4.62	17.46	2.42	15.98	18.61	1.96
Zn	0.02	6.29	5.63	6.65	6.74	5.49	5.53	6.78	2.04	5.57	4.00	5.50	2.03	1.56	5.40
S	0.01	24.93	25.24	26.83	26.57	25.01	24.91	27.64	28.07	25.35	27.92	24.98	28.07	27.91	24.64
Pb	0.03	0.38	0.52	<	<	0.84	0.18	0.11	0.07	0.71	0.04	0.41	<	0.05	0.35
Bi	0.03	<	<	1.41	1.41	<	0.33	1.15	<	<	<	<	0.31	0.05	<
Sb	0.03	26.07	24.07	8.33	9.28	24.35	25.87	7.04	0.70	21.52	4.07	25.99	4.22	0.62	26.61
Ag	0.02	0.06	<	0.04	<	0.03	<	0.03	<	0.05	<	0.05	0.04	0.03	0.05
Cd	0.03	0.04	0.03	0.04	0.06	<	0.09	0.04	0.07	0.07	0.07	0.13	0.08	<	0.10
Cu	0.02	39.24	40.18	42.55	42.44	40.45	39.79	42.72	47.22	41.04	45.62	40.21	46.15	47.12	39.71
Fe	0.01	1.15	1.43	0.99	0.78	1.21	1.56	1.00	2.83	1.59	1.88	1.62	2.98	2.98	1.70
Total		100.02	100.61	100.35	99.56	100.37	100.50	100.96	99.20	100.52	101.08	101.31	99.86	98.94	100.53
Calculated based on 29 atoms															
Cu		10.21	10.31	10.32	10.41	10.45	10.31	10.19	11.05	10.44	10.67	10.34	10.88	11.07	10.33
Ag		0.01	-	0.01	-	0.00	-	0.00	-	0.01	-	0.01	0.00	0.00	0.01
Fe		0.34	0.42	0.27	0.22	0.36	0.46	0.27	0.75	0.46	0.50	0.47	0.80	0.80	0.50
Zn		1.59	1.40	1.57	1.61	1.38	1.39	1.57	0.46	1.38	0.91	1.37	0.46	0.36	1.37
Cd		0.01	0.00	0.00	0.01	-	0.01	0.01	0.01	0.01	0.01	0.02	0.01	-	0.02
As		0.41	0.76	2.78	2.55	0.66	0.49	2.93	3.61	1.00	3.46	0.53	3.19	3.71	0.43
Sb		3.54	3.22	1.05	1.19	3.28	3.50	0.88	0.08	2.86	0.50	3.49	0.52	0.08	3.61
Bi		-	-	0.10	0.11	-	0.03	0.08	-	-	-	-	0.02	0.00	0.00
Pb		0.03	0.04	-	-	0.07	0.01	0.01	0.01	0.06	0.00	0.03	-	0.00	0.03
S		12.86	12.84	12.89	12.91	12.81	12.79	13.07	13.02	12.79	12.95	12.73	13.11	12.99	12.70

Notes: Ttr–Tetrahedrite; Ten–tennantite; <–below minimum limit of detection.

**Table 5.** Element substitution induced increase/decrease of reflectance for Fe-bearing minerals

Mineral	Formula	Reflectance (%)	Increase of reflectance	Decrease of reflectance	References
Magnetite	FeFe <sub>2</sub> O <sub>4</sub>	20–21		Si <sup>4+</sup> (Fe <sup>3+</sup> ), Al <sup>3+</sup> (Fe <sup>3+</sup> ), Ca <sup>2+</sup> (Fe <sup>2+</sup> ), Mg <sup>2+</sup> (Fe <sup>2+</sup> )	Criddle and Stanley 1993; This study
Garnet (andradite-grossular series)	Ca <sub>3</sub> (Fe, Al) <sub>2</sub> Si <sub>3</sub> O <sub>12</sub>	~9 for andradite	Fe <sup>3+</sup> (Al <sup>3+</sup> )		This study
Wolframite	(Fe, Mn) WO <sub>4</sub>	15~16 for huebnerite	Fe <sup>2+</sup> (Mn <sup>2+</sup> )		This study
Tetrahedrite-tennantite	Cu <sub>6</sub> (Cu <sub>4</sub> (Fe, Zn) <sub>2</sub> )(Sb, As) <sub>4</sub> S <sub>13</sub>	31–33	Fe <sup>3+</sup> (Cu <sup>2+</sup> ), Zn <sup>2+</sup> (Cu <sup>2+</sup> ), Ag <sup>+</sup> (Cu <sup>+</sup> )	As <sup>3+</sup> (Sb <sup>3+</sup> )	Hall et al. 1974, This study
Pyrite	FeS <sub>2</sub>	36–55		As <sup>3+</sup> (Fe <sup>2+</sup> ), As <sup>1-</sup> (S <sub>2</sub> <sup>2-</sup> ), Co <sup>2+</sup> (Fe <sup>2+</sup> ), Ni <sup>2+</sup> (Fe <sup>2+</sup> )	Vaughan 1969; Zhu et al. 2021
Sphalerite	ZnS	16–17	Fe <sup>2+</sup> (Zn <sup>2+</sup> )		Awadh 2009; Lai et al., 2023
Chromite	FeCr <sub>2</sub> O <sub>4</sub>	13–17	Fe <sup>3+</sup> (Cr <sup>3+</sup> )	Al <sup>3+</sup> (Cr <sup>3+</sup> )	Eales 1980; López-Benito et al. 2017
Goethite	FeO(OH)	15–17		Si <sup>4+</sup> (Fe <sup>3+</sup> ), Al <sup>3+</sup> (Fe <sup>3+</sup> )	Donskoi et al. 2022
Ilmenite	FeTiO <sub>3</sub>	17–20		Mg <sup>2+</sup> (Fe <sup>2+</sup> )	Cervelle et al. 1971

Note: reflectance values of minerals (at 589 nm in air) are from Criddle and Stanley (1993) and Stanley (2013); elements in brackets were replaced by elements outside.